Optics Communications 451 (2019) 361–366

Contents lists available at ScienceDirect

Optics Communications

journal homepage: www.elsevier.com/locate/optcom

Wedge prism assisted quantitative phase imaging on standard microscopes

Muhammed Fatih Toy *

Department of Biomedical Engineering, School of Engineering and Natural Sciences, Istanbul Medipol University, 34810, Turkey
Center for Novel Microscopy Technologies, Istanbul Medipol University, 34810, Turkey

ARTICLE INFO

Keywords:
Microscopy
Phase imaging
Holography

ABSTRACT

Adoption of quantitative phase imaging for biomicroscopy applications has been limited due to the technical knowledge requirements or the cost of commercial systems. Here, a wedge prism based simple approach is introduced to acquire quantitative phase images on a standard microscope. The proposed approach minimizes the alignment requirements and the cost. Acquired quantitative phase images reflect the sample morphology and the refractive index. Hence, it enables quantitative microscopy without the need for labeling. Optimization parameters are explored for the physical constraints of the cameras and microscope objectives. Experimental quantitative phase images are provided for the USAF-1951 test target, epithelial cell samples, and microsphere samples. Cell imaging results demonstrate the qualitative performance in an exemplary scenario. Quantitative phase imaging of microsphere samples provides experimental proof for the preservation of the resolving power.

1. Introduction

Quantitative phase imaging (QPI) represents a family of imaging technologies that can extract the optical phase retardation map of a sample [1]. Some of these technologies rely on the interferometric imaging principle [2–5], while others may rely on classical transport of intensity [6,7], ptychography [8], or change in aberration [9]. Within the group of interferometric approaches, off-axis digital holography has been one of the most utilized techniques [10–12]. Depending on the type of the imaging as being either transmission or reflection, most commonly a Mach–Zehnder or a Michelson interferometer is utilized with a slight off-axis between the sample and the reference arm of the interferometer. The set of advantages as being label-free, noninvasive, fast, comprehensible, and quantitative has been a driving force behind the increasing popularity of QPI in the biomicroscopy. However, the adoption of QPI in the routine biology research has been limited. The requirement of expertise in optics to realize a quantitative phase microscope can be accounted as a reason for this situation. On an alternative route, a commercial quantitative phase or digital holographic microscope can be acquired by the biology-oriented research groups. In this case, the cost may be prohibitive to assess the potential of QPI. As a third alternative, an existing microscope can be upgraded to acquire quantitative phase images. Numerous approaches have been proposed to realize an upgrade of this kind. Sparsity within the imaged field of view is exploited in a group of methods. An empty region within the field of view is redirected as a reference beam of an interferometer in these methods [13–26]. In another group of methods, a duplicate of the object diffracted field is spatially filtered or modified in a controlled fashion and recombined with the original to form a hologram of a specific type [27–33]. Requirements on the expertise in optics are relaxed with these systems. However, they are still composed of multiple optical elements, which require alignment and a certain level of investment. Early classical off-axis holography setups follow the simplest configuration with a displaced wedge prism on the object plane for the recording of Fresnel holograms [34] or the displaced prism resides on the lens plane of a 2-f imaging system in the case of Fourier holograms [35].

Here I introduce the implementation of a simple shearing interferometer for off-axis holography employing a custom wedge prism on the image plane of a commercial microscope. The implemented shearing interferometer scheme is based on the original off-axis holography proposal of Leith and Upatnieks [34]. The proposed approach eliminates the requirement of additional optical elements while the number of mechanical elements are minimized. Additionally, for further simplification and cost-effectiveness, the wedge prism is built from consumables that can be abundantly found in a research laboratory. Such construction permits the realization of an optimal prism that preserves the optical resolution of the preceding microscope.

2. Wedge prism assisted quantitative phase imaging

2.1. Experimental concept for off-axis carrier fringe pattern generation

Core element of the system, the wedge prism, is constructed from two rectangular microscope cover glasses and liquid optical adhesive

* Corresponding author at: Department of Biomedical Engineering, School of Engineering and Natural Sciences, Istanbul Medipol University, 34810, Turkey.
E-mail address: mftoy@medipol.edu.tr.

https://doi.org/10.1016/j.optcom.2019.07.010
Received 30 April 2019; Received in revised form 4 July 2019; Accepted 7 July 2019
Available online 10 July 2019

between them. Fig. 1(a) illustrates the structure of the wedge prism. A V-shaped cavity is formed between the cover glasses, and it is filled by the optical adhesive. Apex angle of the cavity, α, can be adjusted to maintain a desired beam deviation angle, θ, prior to the curing of the optical adhesive. The details are provided in Section 2.2. The prism is positioned at the image plane of the camera port of an inverted microscope. It covers the half of the field of view with the thick and long edge of it passing through the center of the field of view. The prism is oriented at 45° with the horizontal for an optimal interference fringe sampling on an upright camera. The orientation of the prism in the field of view is shown in Fig. 1(b). An illustration of the entire system is given in Fig. 1(c).

Illumination form a coherent source (LD) is collimated by a lens (CL). The collimated beam illuminates a sample positioned on the sample plane (SP) of the microscope. The light scattered by the sample is collected by a microscope objective (MO) and guided in the inverted microscope's body that is illustrated by the dashed gray box in Fig. 1(c). Within the body, a tube lens (TL) and a motorized folding mirror (FM) aid the formation of an image on the image plane (IP) of the camera port (CP) of the microscope. The wedge prism (WP) is positioned on this image plane. A monochrome digital camera is positioned away from the image plane. Half of the sample plane is denoted with the letter "O" to indicate an object of interest may lay in this half of the illuminated area. Meanwhile the other half is marked as the reference with the letter "R". The reference area is required to be free of any sample. Respectively, the images of these regions are formed on the image plane in the halves indicated by "O′" and "R′". Object region propagates after the image plane with no perturbation and reaches to the camera. However, the other half is refracted by the wedge prism towards O′ at an angle of θ. The interference pattern between the out of focus R′ and O′ is recorded by the camera.

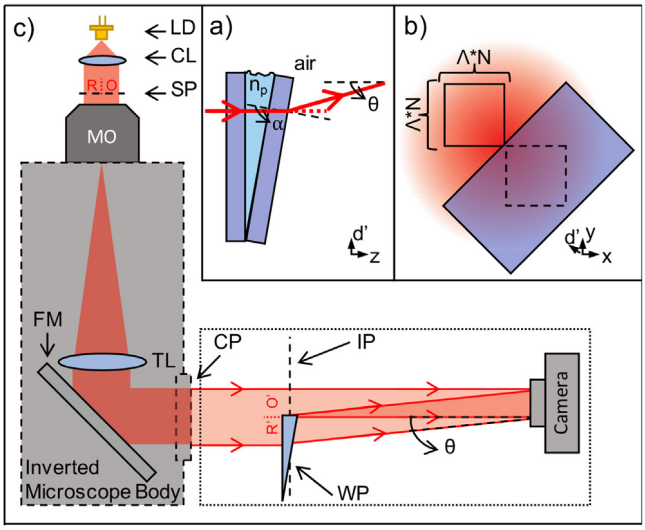

Fig. 1. Wedge prism and the experimental setup. (a) Cross section of the wedge prism constructed from two microscope cover glasses (sky blue colored rectangles) and liquid optical adhesive (maya blue). Red lines represent principal propagation direction of light. (b) Orientation of the wedge prism on the image plane. A uniform gaussian illumination is shown in red, blue colored rectangle represents the wedge prism. Black square outline demonstrates the projected outline of the camera sensor. (c) An overview of the entire system. The add-on to the commercial microscope is outlined by the black dotted rectangle. (LD: Laser diode, CL: Collimating lens, SP: Sample plane, O: Object, R: Reference, MO: Microscope objective, TL: Tube lens, FM: Folding mirror, CP: Camera port, IP: Image plane, WP: Wedge prism, O′: Object image, R′: Reference image).. (For interpretation of the references to color in this figure legend, the reader is referred to the web version of this article.)

2.2. Construction of the wedge prism

Two rectangular microscope slides are placed vertically with their long edges in contact and on a planar surface. The topside long edge separated to maintain the desired wedge angle of α. In this configuration, vertical short edges are sealed using poster putty (Faber-Castell, Tack It), and a wedge-shaped cavity is formed between the microscope slides. The cavity in between the coverslips is filled with the liquid optical adhesive (Norland, NOA65) by capillary action. NOA65 is chosen due to its refractive index (1.524) being approximately equal to the refractive index of the soda lime microscope slides. Subsequently, the adhesive is cured under ultraviolet light, and the seals are removed.

2.3. Lateral resolution

Following a nonlinear hologram filtering method, the interference angle, θ, for optimal hologram sampling on camera can be expressed as $\theta = \sin^{-1}[\lambda/(\Lambda 2\sqrt{2})]$ as a function of wavelength, λ, and the camera pixel size, Λ [36]. Under such conditions, numerical aperture on the camera plane (NA_{im}) is ultimately limited as $NA_{im} \leq \lambda/(4\Lambda)$. For a configuration, with a wavelength of 660 nm and the Basler 102f model camera having pixels at 6.45 μm of size, desired θ angle is calculated to be 2.073°. Snell's law may be utilized to calculate the apex angle for a given interference angle as (1) under the assumption of the refractive indices of the microscope slides and the optical adhesive are equal to each other, n_p, for the refraction condition illustrated in Fig. 1(a).

$$\alpha = \tan^{-1}\left(\frac{\sin\theta}{n_p - \cos\theta}\right) \tag{1}$$

Calculated θ angle value along with the refractive index of soda lime glass at 660 nm of wavelength (1.5207) results in an α angle of 3.969°. One may also apply small angle approximation for a more compact expression, $\alpha \approx \theta/(n_p - 1)$. Calculated optimal apex angle is directly utilized for the construction of the wedge prism by adapting the thickness of the spacer separating the microscope slides.

The distance between the image plane and the camera, s, is required to be as short as possible to maximize the numerical aperture, while maintaining the interference fringes on the entire sensor area. Referring to Fig. 1(b), where the image plane is illustrated with the projection of camera sensor outlined with the black square, the interfering reference region is required to be emerging from the dashed square to maintain s as short as possible. In this approach, influence of the diffraction artifacts emerging from the prism edge are neglected. Analytically, the distance s can be expressed as

$$s = \frac{N\Lambda\sqrt{2}}{\tan\theta} \tag{2}$$

for a square shaped image sensor with a number of pixels, N, on an axis. S can be approximated as $s \approx 4N\Lambda^2/\lambda$ for the optimal θ angle under the small angle approximation. Using a fixed s distance, one may reach to a numerical aperture (NA_{im}) expression for a point at the center in the image space as follows.

$$NA_{im} = \frac{N\Lambda}{\sqrt{4s^2 + N^2\Lambda^2}} \tag{3}$$

For an imaging sensor with the pixel size of 6.45 μm and the pixel count of 1024×1024 pixels, optimal s distance of 258 mm yields in to a NA_{im} of 0.0128. This NA is required to satisfy $NA_{im} \geq NA_{mo}/M$, in order not to limit the resolution of the microscopy system. In the expression, numerical aperture of a microscope objective in use is given with NA_{mo}. M stands for the magnification of this microscope objective.

The NA_{im} expression can be further simplified under small angle approximation at the optimal θ angle and s distance to $NA_{im} \approx \lambda/(8\Lambda)$. It can be concluded from this equation that a smaller camera pixel size yields in higher NA in the image space. From this perspective, the change of the image space NA with respect to pixel size is presented in Fig. 2 by utilizing (3) and the optimal conditions. On top of the plot, NA to magnification ratios are marked with arrows for several

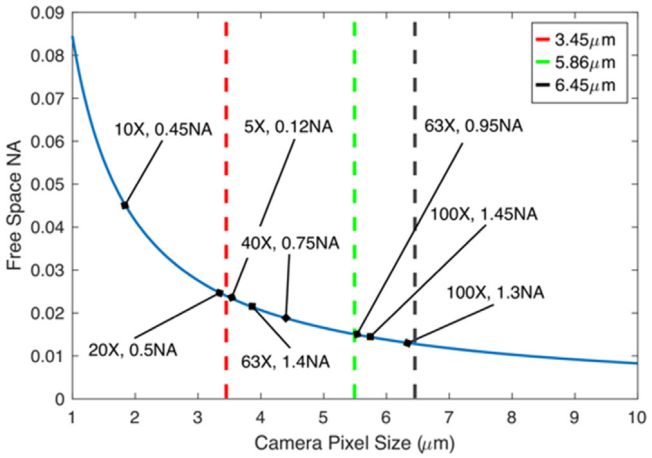

Fig. 2. Maximum free space NA that can be supported by a digital camera based on its pixel size. Image space NA for various common microscope objectives are marked with square arrowheads on the plot. Three pixel sizes as 3.45 μm, 5.86 μm and 6.45 μm are marked with vertical dashed lines in red, green, and black in respective order. . (For interpretation of the references to color in this figure legend, the reader is referred to the web version of this article.)

common microscope objectives. For instance, a microscope objective with 0.45NA and 10X magnification requires an image space NA of at least 0.045. From the plot this NA can be translated to the requirement of a camera pixel size of maximum 1.84 μm.

The presented lateral resolution analysis assumes that the coherent light source has a sufficiently long coherence length to maintain interference for the entire camera sensor area. Considering that the image of the reference region propagates through the wedge prism and gets refracted, the optical path of the reference is longer than the object region. The largest optical path length difference between them, d_{max}, can be approximated as

$$d_{max} \approx h\left(n_p - 1\right)\tan\alpha + s\left(\frac{1}{\cos\theta} - 1\right) \tag{4}$$

for a wedge prism with height, h. This calculation includes the path length difference due to propagation in the prism in the first term. Second term expresses the optical path length difference due to the refracted propagation from the image plane to the camera sensor. Shortest permissible coherence length of the light source is required to be equal to d_{max}.

2.4. System parameters for different camera sensors

Three common pixel sizes as 6.45 μm, 5.86 μm, and 3.45 μm are marked with vertical dashed lines on Fig. 2. Square arrowheads falling to the right of each dashed line satisfy the NA requirement for that specific pixel size. As it can be concluded from the figure, 3.45 μm pixel size supports most of the marked microscope objectives. Meanwhile, a pixel size of 6.45 μm barely limits the performance of one microscope objective (100X 1.3NA) while significantly reducing of the others.

Based on the presented equations and experimental conditions, all of the required parameters for the three different pixel sizes are calculated. These parameters are presented in Table 1. The choice of these pixel sizes is based on the imaging sensors commonly used in cameras. Smaller pixel size in the same effective field of view in comparison to a larger one requires a shorter image plane to camera distance on top of the aforementioned free space NA improvement.

The recorded interference pattern is in the form of an off-axis hologram. Hence, it can be reconstructed like any other off axis hologram. Classically a two-step procedure of first spatial filtering and then numerical propagation is employed [37,38]. Here, the propagation distance is equal to s in magnitude, which is comparably larger than a typical out of focus distance of a holographic microscope.

Table 1
Calculated parameters for various camera sensors. optimal wedge prism apex angle (α), interference angle (θ), free space numerical aperture (NA), and wedge prism to camera sensor distance (s) values are provided for various camera sensor models for various crop sizes (N).

Sensor model	Pixel size (μm)	N × N	θ (°)	α (°)	NA	s (mm)
Sony ICX285	6.45	512 × 512 1024 × 1024	2.073	3.969	0.0128	129.01 258.02
Sony IMX174	5.86	512 × 512 1024 × 1024	2.282	4.366	0.0141	106.47 212.94
Sony IMX250	3.45	512 × 512 1024 × 1024 2048 × 2048	3.878	7.369	0.0240	36.85 73.70 147.40

2.5. Optical setup

A Zeiss Axio Observer 7 inverted microscope hosts the wedge prism on its right-side camera port. For the classical bright field imaging comparison, a monochrome digital camera (Pco.edge 4.2) is attached on the left-side camera port. A battery powered low power laser diode (Thorlabs L650P007) at 660 nm of wavelength serves as the coherent illumination source. The light source is mounted in place of the transillumination condenser of the microscope. For the collimation of the laser beam, an aspherical lens with 4.51 mm focal length (Thorlabs, C230TME-A) is mounted right under the laser diode. Wedge prism is attached on standard optomechanical mounts and positioned at the image plane of the right-side camera port. Two different monochrome digital cameras (Basler A102fm and IDS UI-3080CP-M-GL) are employed. Basler A102fm is based on Sony ICX285AL CCD imaging sensor with 1392×1040 pixels at the size of 6.45 μm. A region of 1024×1024 pixels is used for hologram acquisition on this model. A Sony IMX250 CMOS imaging sensor is hosted inside IDS UI-3080CP-M-GL. This sensor has 3.45 μm sized 2456×2054 pixels. A crop region of 2048×2048 pixels is chosen for this camera model. Two different microscope objectives are utilized for the imaging. A 40X 0.75NA objective (Zeiss EC Plan-Neofluar 40X 0.75NA) is employed along with Basler 102fm camera for the imaging of USAF-1951 test target and epithelial cells. Microspheres are imaged through a 63X 1.4NA objective (Zeiss Plan-Apochromat 63X 1.4NA) on the IDS UI-3080CP-M-GL camera.

2.6. Sample preparation

Three different samples are imaged on the experimental setup. The first sample is a positive USAF-1951 test target (Edmund Optics #58–198). The test target is placed on the sample plane in focus with no preparation. Epithelial cells are harvested from the buccal region of the author using a cotton-tipped bamboo stick and then transferred on to a #1.5 coverslip for imaging. Polystyrene microspheres are acquired in the form of aqueous suspension (2.5% solids w/v) from Polysciences, Inc (Polybead® microspheres cat07307, Mean diameter = 0.465 μm). Microsphere suspension is diluted in DI water with the dilution ratio of 1:100. A drop of the diluted suspension is transferred on to a #1.5 coverslip with the addition of isopropyl alcohol at the same amount. The sample is mounted on the microscope sample stage after the evaporation of DI water.

3. Results and discussion

In the experimental part, the design of the setup is initially based on a camera with pixel size of 6.45 μm. Respectively, wedge prism parameters and the s distance are optimized for 1024×1024 array size. A USAF-1951 test target is imaged. The acquired hologram is presented in Fig. 3(a). The white dashed box shows the zoomed in central region. The diagonal fringe orientation is evident from this inset. The distance between the fringes can be exploited to verify the θ angle. A more accurate calculation of θ angle is based on the Fourier transform of the

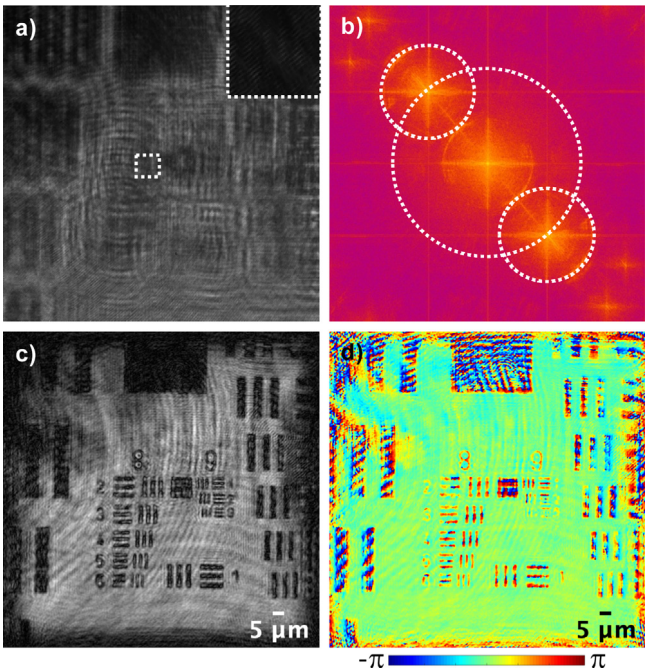

Fig. 3. Acquired sample hologram with reconstructed amplitude and quantitative phase images. (a) An experimental hologram of a USAF-1951 resolution test target, and (b) its Fourier transform in log scale. The boundaries of passband regions are highlighted with white dashed circles. The numerical reconstruction of the hologram yields in the amplitude (c) and phase (d) images.

hologram that is shown in Fig. 3(b). The distance between the zeroth order and the first order diffraction reflects the actual θ angle with higher accuracy. This calculation results in an experimentally realized prism's θ angle of 1.717°. Amplitude and phase images reconstructed from the hologram are shown in Fig. 3 (c and d). Target structures are well resolvable in both images. The employed microscope objective has 40X magnification with 0.75 NA. However, this imaging performance is limited by the wedge prism. The experimental θ angle requires a larger than ideal s distance of 311.6 mm and confines the free space NA to 0.0106. This free space NA translates into an object space NA of 0.424 which ultimately limits the resolution. Under these circumstances, the coherent Rayleigh resolution limit corresponds to 1.28 μm. The smallest features on the test target have the periodicity of 1.56 μm. This conclusion agrees with the aforementioned observation on the amplitude and phase images. Both amplitude and phase images in Fig. 3 express some degree of noise on their background. For the specific case of the USAF-1951 test target, reference region on the image plane is not free of perturbations and contains some target features. Eventually, this non-ideal reference region results in the observable noise. After this initial performance verification experiment, unstained buccal epithelial cells are imaged on the microscope. Phase images of these cells are shown on Fig. 4. Two different fields are given in the sub panels. Cellular morphology, nuclei, and internal structures are well observable for both of the fields.

For a second phase of experiments another camera with smaller pixels at the size of 3.45 μm is employed. A new wedge prism is constructed with the targeted θ angle presented in Table 1. Following the previously explained characterization routine, the experimental θ angle is measured as 4.345°. This angle yields in a critical s distance of 131.5 mm and the free space NA of 0.0269. At this free space NA, all of the microscope objectives marked in Fig. 2 except one (10X 0.45NA) can be employed without resolution degradation. Polystyrene microspheres at known sizes are imaged in order to demonstrate the resolution performance for phase dominant type objects. Microspheres with the mean diameter of 0.465 μm are imaged with the help of 63X 1.4NA oil immersion objective. A region with two microspheres in contact is chosen for a better evaluation of resolution. Fig. 5(a) shows an ordinary brightfield microscopy image of this region of interest. In the reconstructed quantitative phase image for the same region, individual microspheres are resolvable, Fig. 5(b). Phase imaging performance assessment is based on the theoretical expectations. Expected phase retardation profile is calculated for two microspheres with the size of mean diameter and in contact. This calculation also includes the effect of magnification and the numerical aperture limit of the employed microscope objective. Red trace in Fig. 5(c) demonstrates this theoretical phase profile. The phase profile in between the red arrowheads in Fig. 5(b) is compared to the theoretical profile. The experimental phase profile in blue in Fig. 5(c) expresses high similarity to the theory both in the maximal values and the valley in between the microspheres. The microspheres observable at the top region of Fig. 5(b) express an inverted phase response in comparison to the microspheres of interest. An object existing in the reference region of a shearing interferometer expresses an inverted phase signal in comparison to another object in the object region. A similar type of signal inversion is also observable on the earlier examples of quantitative phase imaging add-on modules [23].

In order to evaluate the temporal performance of the setup, a blank coverslip is loaded to the sample stage. A total of 150 holograms are recorded at the acquisition rate of 100 frames /sec. Each hologram is independently processed to reconstruct phase images. On these phase images, a region of 500×500 pixels is chosen. At each pixel location, the temporal standard deviation of optical path length is calculated. Mean of the standard deviations from the entire region results into 2.36 nm of temporal optical path length noise. This temporal noise performance is inferior to the other common path interferometer-based QPI systems with reported values are typically less than 1 nm [2,15,16,19–22,30,32] and reaching to values less than 0.2 nm in some cases [25,29]. The light source and the environmental disturbances can be counted as the possible origins of this comparably large temporal noise of the proposed system. Coherent noise and the mode hopping of the non-thermo-regulated laser diode employed as the light source are some possible light source related noise sources. On top of this, spatial to temporal noise mixing due to vibrations and large out of focus distance can be held responsible for the temporal phase noise.

Alignment of the interferometric optical setups generally require high precision manipulators for either positional or angular adjustments. Such setups are commonly prone to misalignment due environmental factors like thermal gradients. Some interferometric approaches (e.g. shearing interferometers) are robust against environmental factors and does not require high precision adjustment, but typically lack the flexibility of the other methods. Here, only two elements, the wedge prism and the camera require alignment for the initial positioning. Having both of these elements in the image side further relaxes their alignment tolerances. Hence, they can be positioned without the need of a special tool. Due to the same reasons, optical setup is robust against the misalignment of these elements with varying environmental factors. The fundamental layout of the optical setup brings some intrinsic limitations to the imaging capabilities. As expressed in Section 2.1, a neighboring region next to the imaged sample is required to be free of samples and perturbation. This region serves as the reference beam of the interferometer. This condition limits the application of the system to the sparse sample. Hence, extended samples like tissue section slices or confluent cell cultures are not suitable for imaging on this platform. Refractive nature of the prism-based architecture brings a limitation on the coherence length of the employed light source. For the experimental conditions presented here, millimeter scale coherence length of the light source is required to have interference on the entire field of view. Hence the light source is required to have adequately narrow spectral width, e.g. laser diodes, and diode pumped solid state lasers. This condition prohibits the use of a superluminescent diode or a light emitting diode as the light source in the presented configuration. Additionally,

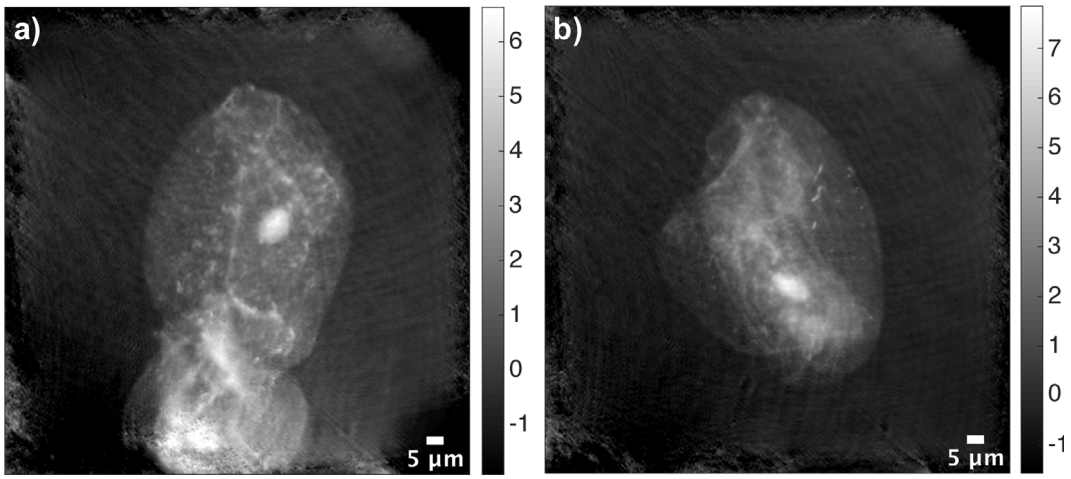

Fig. 4. Quantitative phase images of buccal epithelial cells. (a and b) Buccal epithelial cells are imaged on the developed system. Reconstructed quantitative phase images for two different regions are provided. (Phase values are in radians.)

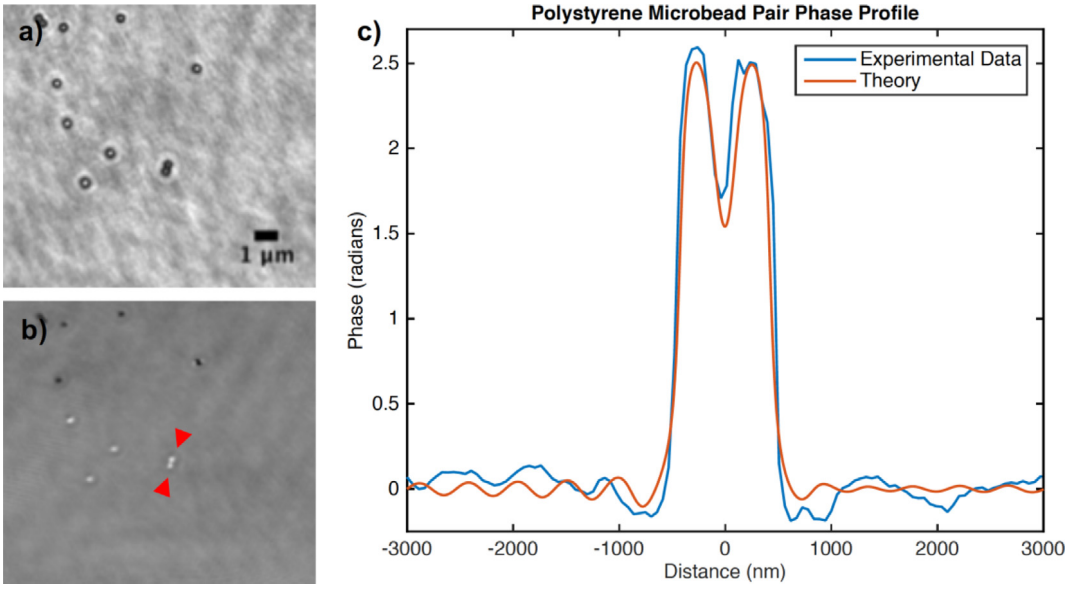

Fig. 5. Quantitative phase imaging of microbeads. (a) Brightfield image of a region with multiple microspheres. (b) Quantitative phase image of the same region given in panel (a). Red arrowheads show a pair of 0.465 µm sized beads in contact. (c) Comparison of the theoretical phase profile of two microspheres (in red) to the experimental profile (in blue) extracted from panel (b) between the red arrowheads. . (For interpretation of the references to color in this figure legend, the reader is referred to the web version of this article.)

employed nonlinear filtering technique requires a higher intensity on the reference region in comparison to the object region. In the case of weakly scattering samples (e.g. low confluency cell cultures), this requirement is sufficiently relaxed to yield in negligible artifacts. For the strong scattering samples, the higher intensity requirement for the reference region can be satisfied by the displacement of the illumination beam center towards to the reference region. Besides, the long distance between the microscope image plane and the camera causes the acquired sample hologram to be largely out of focus. In spite of the existence of numerical refocusing capability, this situation may slow down the procedure of searching for a region of interest. Observation through the ocular of the microscope or the use of an additional camera for classical brightfield imaging can be considered to speed up the region of interest search. As a future improvement, a custom lamp house hosting both the brightfield white light source and the coherent light source, which enables the use of a single condenser lens for both of the sources, can potentially further simplify the integration of the proposed concept and enable fast switching between the two modes of operation.

4. Conclusions

Here, I demonstrated a simple approach to enable quantitative phase imaging on an ordinary microscope. The approach relies on the use of an easy to construct wedge prism on the image plane of the microscope. A digital camera was positioned after the wedge prism at a distance where the interference was observable on the entire sensor area. The acquired interference pattern was treated as an ordinary off-axis hologram to reconstruct amplitude and quantitative phase images. Three different microscopic objects (a resolution test target, cell sample, and transparent microspheres) were imaged. Results demonstrated that QPI is easily attainable for sufficiently sparse samples without any degradation in the resolving power. This research can open up many opportunities for the use of quantitative phase microscopy in cellular imaging, microelectromechanical systems, and microfluidic systems.

Acknowledgments

This work was supported in part by the Istanbul Development Agency (ISTKA), Innovative and Creative Istanbul Financial Support Program 2016 (Project Number: TR10/16/YNY/0033).

Appendix A. Supplementary data

Supplementary material related to this article can be found online at https://doi.org/10.1016/j.optcom.2019.07.010.

References

[1] G. Popescu, Quantitative Phase Imaging of Cells and Tissues, McGraw-Hill, New York, 2011.
[2] G. Popescu, T. Ikeda, R.R. Dasari, M.S. Feld, Diffraction phase microscopy for quantifying cell structure and dynamics, Opt. Lett. (2006) http://dx.doi.org/10.1364/ol.31.000775.
[3] B. Kemper, D. Carl, A. Höink, G. von Bally, I. Bredebusch, J. Schnekenburger, Modular digital holographic microscopy system for marker free quantitative phase contrast imaging of living cells, Proc. SPIE 6191 (2006) 61910T.
[4] P. Marquet, B. Rappaz, P.J. Magistretti, E. Cuche, Y. Emery, T. Colomb, C. Depeursinge, Digital holographic microscopy: a noninvasive contrast imaging technique allowing quantitative visualization of living cells with subwavelength axial accuracy, Opt. Lett. (2005) http://dx.doi.org/10.1364/ol.30.000468.
[5] W. Choi, C. Fang-Yen, K. Badizadegan, S. Oh, N. Lue, R.R. Dasari, M.S. Feld, Tomographic phase microscopy, Nature Methods (2007) http://dx.doi.org/10.1038/nmeth1078.
[6] L. Waller, L. Tian, G. Barbastathis, Transport of intensity imaging with higher order derivatives, Opt. Express (2010) http://dx.doi.org/10.1364/oe.18.012552.
[7] S.S. Kou, L. Waller, G. Barbastathis, C.J.R. Sheppard, Transport-of-intensity approach to differential interference contrast (TI-DIC) microscopy for quantitative phase imaging, Opt. Lett. (2010) http://dx.doi.org/10.1364/ol.35.000447.
[8] J. Marrison, L. Räty, P. Marriott, P. O'Toole, Ptychography-a label free, high-contrast imaging technique for live cells using quantitative phase information, Sci. Rep. (2013) http://dx.doi.org/10.1038/srep02369.
[9] L. Waller, S.S. Kou, C.J.R. Sheppard, G. Barbastathis, Phase from chromatic aberrations, Opt. Express (2010) http://dx.doi.org/10.1364/oe.18.022817.
[10] E. Cuche, F. Bevilacqua, C. Depeursinge, Digital holography for quantitative phase-contrast imaging, Opt. Lett. (1999).
[11] Y. Cotte, F. Toy, P. Jourdain, N. Pavillon, D. Boss, P. Magistretti, P. Marquet, C. Depeursinge, Marker-free phase nanoscopy, Nat. Photonics (2013) http://dx.doi.org/10.1038/nphoton.2012.329.
[12] J.K. Wallace, S. Rider, E. Serabyn, J. Kühn, K. Liewer, J. Deming, G. Showalter, C. Lindensmith, J. Nadeau, Robust, compact implementation of an off-axis digital holographic microscope, Opt. Express (2015) http://dx.doi.org/10.1364/OE.23.017367.
[13] Y.J. Jo, S. Park, J.H. Jung, J. Yoon, H. Joo, M.H. Kim, S.J. Kang, M.C. Choi, S.Y. Lee, Y.K. Park, Holographic deep learning for rapid optical screening of anthrax spores, Sci. Adv. (2017) http://dx.doi.org/10.1126/sciadv.1700606.
[14] M. Rostykus, C. Moser, Compact lensless off-axis transmission digital holographic microscope, Opt. Express (2017) http://dx.doi.org/10.1364/oe.25.016652.
[15] K. Kim, Z. Yaqoob, K. Lee, J.W. Kang, Y. Choi, P. Hosseini, P.T.C. So, Y. Park, Diffraction optical tomography using a quantitative phase imaging unit, Opt. Lett. (2014) http://dx.doi.org/10.1364/ol.39.006935.
[16] N.T. Shaked, M.T. Rinehart, A. Wax, Dual-interference-channel quantitative-phase microscopy of live cell dynamics, Opt. Lett. (2009) http://dx.doi.org/10.1364/ol.34.000767.
[17] J. Di, Y. Li, M. Xie, J. Zhang, C. Ma, T. Xi, E. Li, J. Zhao, Dual-wavelength common-path digital holographic microscopy for quantitative phase imaging based on lateral shearing interferometry, Appl. Opt. (2016) http://dx.doi.org/10.1364/AO.55.007287.
[18] D. Roitshtain, N.A. Turko, B. Javidi, N.T. Shaked, Flipping interferometry and its application for quantitative phase microscopy in a micro-channel, Opt. Lett. (2016) http://dx.doi.org/10.1364/ol.41.002354.
[19] C. Ma, Y. Li, J. Zhang, P. Li, T. Xi, J. Di, J. Zhao, Lateral shearing common-path digital holographic microscopy based on a slightly trapezoid sagnac interferometer, Opt. Express (2017) http://dx.doi.org/10.1364/oe.25.013659.
[20] A.S.G. Singh, A. Anand, R.A. Leitgeb, B. Javidi, Lateral shearing digital holographic imaging of small biological specimens, Opt. Express (2012) http://dx.doi.org/10.1364/oe.20.023617.
[21] K. Lee, Y. Park, Quantitative phase imaging unit, Opt. Lett. (2014) http://dx.doi.org/10.1364/ol.39.003630.
[22] V. Chhaniwal, A.S.G. Singh, R.A. Leitgeb, B. Javidi, A. Anand, Quantitative phase-contrast imaging with compact digital holographic microscope employing Lloyd's mirror, Opt. Lett. (2012) http://dx.doi.org/10.1364/ol.37.005127.
[23] B. Kemper, A. Vollmer, C.E. Rommel, J. Schnekenburger, G. von Bally, Simplified approach for quantitative digital holographic phase contrast imaging of living cells, J. Biomed. Opt. (2011) http://dx.doi.org/10.1117/1.3540674.
[24] V. Mico, C. Ferreira, Z. Zalevsky, J. García, Spatially-multiplexed interferometric microscopy (SMIM): converting a standard microscope into a holographic one, Opt. Express (2014) http://dx.doi.org/10.1364/oe.22.014929.
[25] S. Ebrahimi, M. Dashtdar, E. Sánchez-Ortiga, M. Martínez-Corral, B. Javidi, Stable and simple quantitative phase-contrast imaging by Fresnel biprism, Appl. Phys. Lett. (2018) http://dx.doi.org/10.1063/1.5021008.
[26] Y. Baek, K. Lee, J. Yoon, K. Kim, Y. Park, White-light quantitative phase imaging unit, Opt. Express (2016) http://dx.doi.org/10.1364/oe.24.009308.
[27] T. Kim, R. Zhou, M. Mir, S.D. Babacan, P.S. Carney, L.L. Goddard, G. Popescu, White-light diffraction tomography of unlabelled live cells, Nat. Photonics (2014) http://dx.doi.org/10.1038/nphoton.2013.350.
[28] T.H. Nguyen, M.E. Kandel, M. Rubessa, M.B. Wheeler, G. Popescu, Gradient light interference microscopy for 3D imaging of unlabeled specimens, Nature Commun. (2017) http://dx.doi.org/10.1038/s41467-017-00190-7.
[29] N.T. Shaked, Quantitative phase microscopy of biological samples using a portable interferometer, Opt. Lett. (2012) http://dx.doi.org/10.1364/ol.37.002016.
[30] P. Girshovitz, N.T. Shaked, Compact and portable low-coherence interferometer with off-axis geometry for quantitative phase microscopy and nanoscopy, Opt. Express (2013) http://dx.doi.org/10.1364/oe.21.005701.
[31] A. Nativ, N.T. Shaked, Compact interferometric module for full-field interferometric phase microscopy with low spatial coherence illumination, Opt. Lett. (2017) http://dx.doi.org/10.1364/ol.42.001492.
[32] S. Mahajan, V. Trivedi, P. Vora, V. Chhaniwal, B. Javidi, A. Anand, Highly stable digital holographic microscope using Sagnac interferometer, Opt. Lett. (2015) http://dx.doi.org/10.1364/ol.40.003743.
[33] R.A. Terborg, J. Pello, I. Mannelli, J.P. Torres, V. Pruneri, Ultrasensitive interferometric on-chip microscopy of transparent objects, Sci. Adv. (2016) http://dx.doi.org/10.1126/sciadv.1600077.
[34] E.N. Leith, J. Upatnieks, Reconstructed wavefronts and communication theory*, J. Opt. Soc. Amer. (1962) http://dx.doi.org/10.1364/josa.52.001123.
[35] A.B. VanderLugt, Signal detection by complex spatial filtering, Institute of Science and Technology, University of Michigan, Ann Arbor, MI, Technical Report (1963).
[36] N. Pavillon, C.S. Seelamantula, J. Kühn, M. Unser, C. Depeursinge, Suppression of the zero-order term in off-axis digital holography through nonlinear filtering, Appl. Opt. (2009) http://dx.doi.org/10.1364/ao.48.00h186.
[37] T. Colomb, E. Cuche, F. Charrière, J. Kühn, N. Aspert, F. Montfort, P. Marquet, C. Depeursinge, Automatic procedure for aberration compensation in digital holographic microscopy and applications to specimen shape compensation, Appl. Opt. (2006) http://dx.doi.org/10.1364/ao.45.000851.
[38] T. Colomb, F. Montfort, J. Kühn, N. Aspert, E. Cuche, A. Marian, F. Charrière, S. Bourquin, P. Marquet, C. Depeursinge, Numerical parametric lens for shifting, magnification, and complete aberration compensation in digital holographic microscopy, J. Opt. Soc. Amer. A (2006) http://dx.doi.org/10.1364/josaa.23.003177.